BIOCHEMISTRY

Molecular mechanisms linking missense ACTG2 mutations to visceral myopathy

Rachel H. Ceron[1,2], Faviolla A. Báez-Cruz[1,3], Nicholas J. Palmer[1,3], Peter J. Carman[1,3], Malgorzata Boczkowska[1], Robert O. Heuckeroth[2,4,5], E. Michael Ostap[1,3]*, Roberto Dominguez[1,3]*

Visceral myopathy is a life-threatening disease characterized by muscle weakness in the bowel, bladder, and uterus. Mutations in smooth muscle γ-actin (ACTG2) are the most common cause of the disease, but the mechanisms by which the mutations alter muscle function are unknown. Here, we examined four prevalent ACTG2 mutations (R40C, R148C, R178C, and R257C) that cause different disease severity and are spread throughout the actin fold. R178C displayed premature degradation, R148C disrupted interactions with actin-binding proteins, R40C inhibited polymerization, and R257C destabilized filaments. Because these mutations are heterozygous, we also analyzed 50/50 mixtures with wild-type (WT) ACTG2. The WT/R40C mixture impaired filament nucleation by leiomodin 1, and WT/R257C produced filaments that were easily fragmented by smooth muscle myosin. Smooth muscle tropomyosin isoform Tpm1.4 partially rescued the defects of R40C and R257C. Cryo–electron microscopy structures of filaments formed by R40C and R257C revealed disrupted intersubunit contacts. The biochemical and structural properties of the mutants correlate with their genotype-specific disease severity.

INTRODUCTION

Visceral myopathies (VMs), including chronic intestinal pseudo-obstruction, pediatric-onset intestinal pseudo-obstruction, and megacystis microcolon intestinal hypoperistalsis syndrome (MMIHS), are a group of rare diseases that often cause death in childhood (*1*–*3*). VM arises from smooth muscle dysfunction in the bowel, bladder, and uterus (*1*). The most common cause of VM is mutations in the gene encoding smooth muscle γ-actin (*ACTG2*) (*4*, *5*). Actin and myosin polymers form the thin and thick filaments of muscle cells that interact and slide past one another during muscle contraction, respectively (*6*). Currently, there are 43 reported heterozygous missense *ACTG2* mutations affecting 31 residues throughout the actin structure (Fig. 1, A and B; fig. S1; and table S1). These mutations are thought to cause disease through dominant-negative rather than loss-of-function mechanisms since heterozygous ACTG2 truncations and frameshifts have been documented in healthy individuals (*1*, *4*, *7*, *8*). Other VM-causing mutations affect genes encoding actin-binding proteins (ABPs) and proteins that regulate muscle contraction, including the actin filament nucleator leiomodin 1 (Lmod1), the smooth muscle myosin heavy and light chains (MYH11 and MYL9), and the myosin light chain kinase (*9*–*12*).

The underlying biochemical and structural mechanisms through which *ACTG2* mutations cause disease have remained elusive, hindering the development of mechanism-based therapies (*13*). One factor contributing to this lack of knowledge is the difficulty of obtaining recombinant ACTG2 protein under native conditions. Using a recently developed actin expression method in human cells (*14*), we analyze wild-type (WT) ACTG2 and four disease-causing mutations (R40C, R148C, R178C, and R257C). Following the standard numbering convention, which is based on α-actin and considers posttranslational processing of the N terminus (*15*, *16*), these residues correspond to R39, R147, R177, and R256 in mature actin. These four residues are the most frequently mutated among patients with VM, affect different areas of the actin structure, and cause different degrees of disease severity (*1*, *4*). Our analysis reveals diverse ways in which the mutations disrupt ACTG2 function, including destabilizing the actin monomer (G-actin), affecting interactions with ABPs, altering polymerization, or interfering with intersubunit contacts within the actin filament (F-actin).

RESULTS

Four representative ACTG2 mutations exhibit varying expression patterns

Mutations of residues R40, R148, R178, and R257 were selected for this study based on their prevalence, collectively accounting for over 70% of reported dominant missense *ACTG2* mutations linked to VM (*1*). Particularly, residue R257 is the most frequently mutated in VM, accounting for 33% of reported cases. While cysteine is a common substitution for these four residues, mutations to other amino acids have also been reported (fig. S1 and table S1). These mutations were additionally selected because they are spread throughout the tertiary structure of G-actin and affect different intersubunit contacts in F-actin (Fig. 1, A and B, and fig. S1). Specifically, R40 forms part of the D-loop (residues R40-K51) that mediates important intersubunit contacts along the long-pitch helix of F-actin and participates in interactions with several ABPs (*17*–*20*). R148 falls near the hydrophobic cleft in actin, which participates in interactions with numerous ABPs and interprotomer contacts in F-actin (*21*, *22*). R148 also forms part of the myosin-binding interface (*23*). R178 is located near the catalytic site and forms part of the back door through which the γ-phosphate is believed to be released after hydrolysis of the actin-bound nucleotide (*19*). Last, R257 forms a salt bridge with E196 and is situated at the interface between adjacent actin subunits of the two long-pitch helices of F-actin. These

[1]Department of Physiology, Perelman School of Medicine, University of Pennsylvania, Philadelphia, PA 19104, USA. [2]The Children's Hospital of Philadelphia Research Institute, Philadelphia, PA 19104, USA. [3]Biochemistry and Molecular Biophysics Graduate Group, Perelman School of Medicine, University of Pennsylvania, Philadelphia, PA 19104, USA. [4]Department of Pediatrics, Perelman School of Medicine, University of Pennsylvania, Philadelphia, PA 19104, USA. [5]Department of Cell and Developmental Biology, Perelman School of Medicine, University of Pennsylvania, Philadelphia, PA 19104, USA.
*Corresponding author. Email: ostap@pennmedicine.upenn.edu (E.M.O.); droberto@pennmedicine.upenn.edu (R.D.)

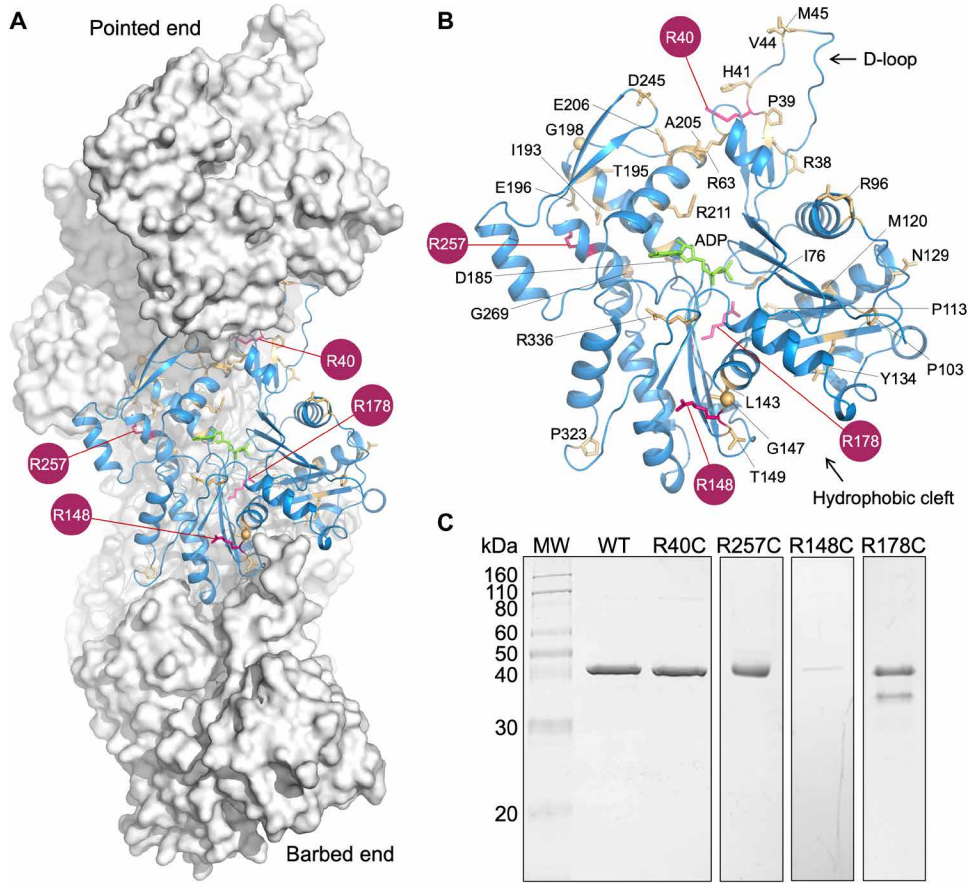

Fig. 1. Choice and purification of ACTG2 mutations for study. (**A**) Surface representation of F-actin [Protein Data Bank (PDB) code: 8F8P] showing a ribbon diagram of a middle subunit (marine blue) with the side chains of ACTG2 residues reported to be mutated in VM displayed in beige or maroon for the four mutations studied here (R40C, R148C, R178C, and R257C). (**B**) Close-up view of the middle subunit shown in (A), highlighting ACTG2 residues reported to be mutated in VM (see also fig. S1 and table S1). The location of the hydrophobic cleft and the D-loop is indicated. (**C**) Coomassie-stained SDS–polyacrylamide gel electrophoresis of purified WT ACTG2 and mutants R40C, R257C, R148C, and R178C (full gels in fig. S2). MW, molecular weight.

mutations are also representative of the spectrum of disease severity (*1*); R178C is associated with the most severe form of VM (*4*), R40C and R257C also cause serious gastrointestinal disease that often presents at birth (*4*), and R148C typically results in later disease onset and relatively mild symptoms (*24*).

Using our previously reported method for actin expression in human Expi293F cells (*14*), we obtained WT ACTG2 and mutants R40C and R257C with high purity and in sufficiently large quantities for structural and biochemical studies (Fig. 1C and fig. S2, A and E). In contrast, we encountered difficulties purifying mutants R148C and R178C, which, while precluding their in-depth analysis, are nonetheless revealing of the mechanisms by which they cause VM. Specifically, R148C was obtained in very low amounts due to weak binding to the affinity column, which uses gelsolin segments 4–6 (G4G6) to bind the expressed actin in a Ca^{2+}-dependent manner (Fig. 1C and fig. S2B; Materials and Methods). As mentioned above, this mutation was expected to affect the binding of ABPs to the hydrophobic cleft in actin, which is the main binding site for G4G6 (*25*). We anticipate that the binding of other ABPs will be similarly affected, likely contributing to this mutant's role in VM. In contrast, R178C could be purified, but unlike other actin isoforms and mutants expressed using this method (*14*), R178C exhibited rapid degradation after purification (Fig. 1C and fig. S2, C and D). The inherent instability of this mutant is proposed to account for its severe VM phenotype.

R40C and R257C alter actin polymerization in different ways

To establish a benchmark for analysis of the mutants, we first compared WT ACTG2 to the extensively studied tissue-purified skeletal α-actin isoform (ACTA1), previously shown to be functionally indistinguishable from recombinant skeletal α-actin obtained using the same method (*14*). Using the pyrene-actin polymerization assay (2 μM total actin, including 6% pyrene-labeled α-actin), WT ACTG2 exhibited slower polymerization compared to α-actin, with polymerization rates of 0.23 and 0.32 nM/s, respectively (Fig. 2, A and D, and table S2). R40C displayed sluggish polymerization, and the rate could only be approximately estimated (Fig. 2, B and D, and table S2). In contrast, R257C polymerized much faster than WT (Fig. 2, C and D, and table S2), although, as shown below, this behavior is likely due to filament fragmentation and the generation of more filament ends.

Because these mutations are heterozygous, we also analyzed 50/50 mixtures of WT/mutant ACTG2, which may more accurately reflect the ratio present in the smooth muscle of patients with

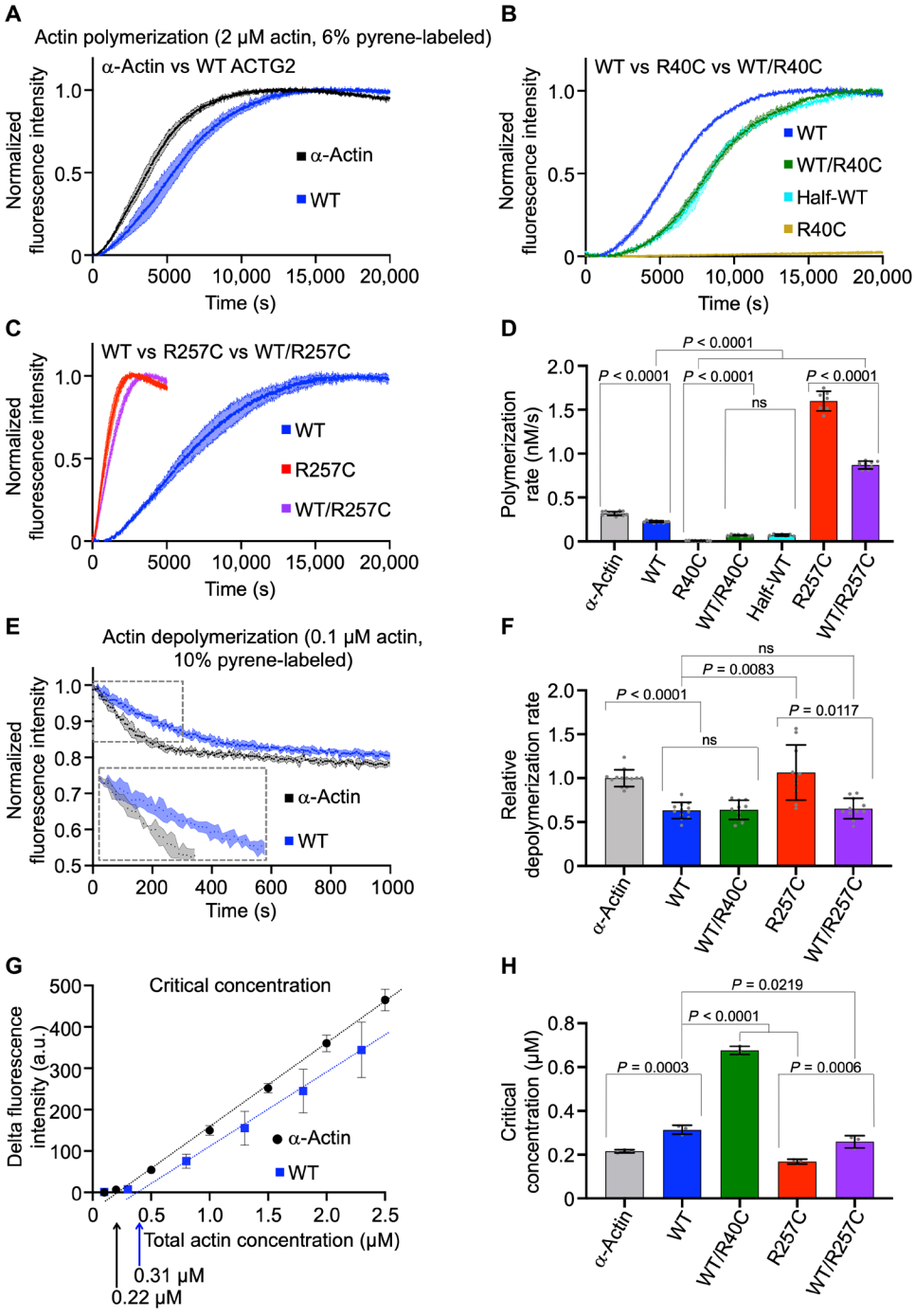

Fig. 2. Mutants R40C and R257C alter actin polymerization in different ways. (**A** to **C**) Time course of actin polymerization (2 µM total actin, including 6% pyrene-labeled α-actin) showing comparisons between WT ACTG2 and α-actin (A); WT, R40C, WT/R40C, and half-WT (1 µM WT ACTG2, 12% pyrene-labeled α-actin) (B); and WT, R257C, and WT/R257C (C). (**D**) Polymerization rates of actin variants calculated from 7–12 reactions using at least three independent actin preparations. (**E**) Example of pyrene-actin depolymerization experiment, showing WT and α-actin. F-actin (10% pyrene-labeled α-actin) is diluted to 0.1 µM (i.e., below the Cc). (**F**) Relative depolymerization rates of actin variants from 11 to 15 reactions using at least three independent protein preparations. Data in (D) and (F) were analyzed by one-way analysis of variance (ANOVA) with Welch's test ($P < 0.0001$), and the P values shown are from Dunnett's T3 multiple comparisons test. (**G**) Example of Cc plots, showing equilibrium fluorescence as a function of the actin concentration (5% pyrene-labeled α-actin) for WT ACTG2 and α-actin. Cc values were calculated from the x intercept of the graphs. a.u., arbitrary units. (**H**) Cc values of actin variants calculated from $n = 3$ independent experiments. Data in (H) were analyzed by one-way ANOVA ($P < 0.0001$), and P values are from Bonferroni's multiple comparisons test. Graphs in (D), (F), (G), and (H) represent means ± SD, with "ns" indicating P values > 0.05.

VM. The WT/R40C mixture polymerized slower than WT but faster than R40C, with a polymerization rate of 0.07 nM s^{-1} (Fig. 2, B and D, and table S2). To test if WT and R40C copolymerized, we also analyzed WT alone but at the concentration and labeling ratio present in the mixture (i.e., 1 μM WT, 12% pyrene-labeled α-actin, referred to as half-WT). The polymerization rate of half-WT matched that of the WT/R40C mixture (Fig. 2, B and D, and table S2), indicating that WT polymerizes mostly alone and that R40C does not contribute to or inhibit filament elongation even when WT filament seeds are present. In contrast, the polymerization rate of the WT/R257C mixture was in between those of WT and R257C, indicating that this mutant copolymerizes with WT and imparts some of its faster polymerization behavior to the mixture (Fig. 2, C and D, and table S2).

The depolymerization rates of ACTG2 variants were determined in experiments where prepolymerized actin filaments were diluted to 0.1 μM total actin (including 10% pyrene-labeled α-actin), which is below the critical concentration (Cc) for polymerization (*26*). Rates are reported for each actin variant individually as well as relative to α-actin (table S2). WT and WT/R40C depolymerized similarly, and both depolymerized slower than α-actin, with rates of 0.63 and 0.64 s^{-1}, respectively, compared to α-actin (Fig. 2, E and F; fig. S3, A and C; and table S2). The depolymerization of R40C could not be analyzed due to its inefficient polymerization. R257C depolymerized faster than WT, whereas WT/R257C depolymerized similarly to WT (Fig. 2F; fig. S3, B and D; and table S2).

To determine the Cc of ACTG2 variants, defined as the monomer concentration at which the polymerization and depolymerization rates are equal (*27*), we measured the equilibrium fluorescence of polymerization reactions at different monomer concentrations (including 5% pyrene-labeled α-actin). Cc values were measured as the *x* intercepts of linear trend lines fitted to plots of fluorescence against the actin concentration. WT ACTG2 exhibited a higher Cc than α-actin (Fig. 2, G and H, and table S2). Although we were unable to measure the Cc of R40C alone, the apparent Cc of the WT/R40C mixture was approximately twice that of WT (Fig. 2H, fig. S3E, and table S2). This observation supports the notion that filaments in this mixture are primarily formed by WT. R257C exhibited a lower Cc compared to WT, and the Cc of WT/R257C fell in between those of R257C and WT, consistent with this mutant copolymerizing with WT (Fig. 2H, fig. S3F, and table S2).

R40C and R257C affect filament nucleation by Lmod1

Lmod1, an actin filament nucleator expressed in smooth muscle cells (*18*, *28*, *29*), is also mutated in some cases of VM (*9*). To assess the impact of ACTG2 mutations on nucleation by Lmod1, we conducted pyrene-actin polymerization assays in the presence of 20 nM Lmod1 (Fig. 3). As anticipated, Lmod1 significantly enhanced the polymerization rate of α-actin and WT ACTG2 (Fig. 3, A and D). While α-actin polymerized faster than ACTG2 with Lmod1, the fold increase in their polymerization rates with Lmod1 was similar when compared to their individual polymerization rates (Fig. 3A and table S2). R40C

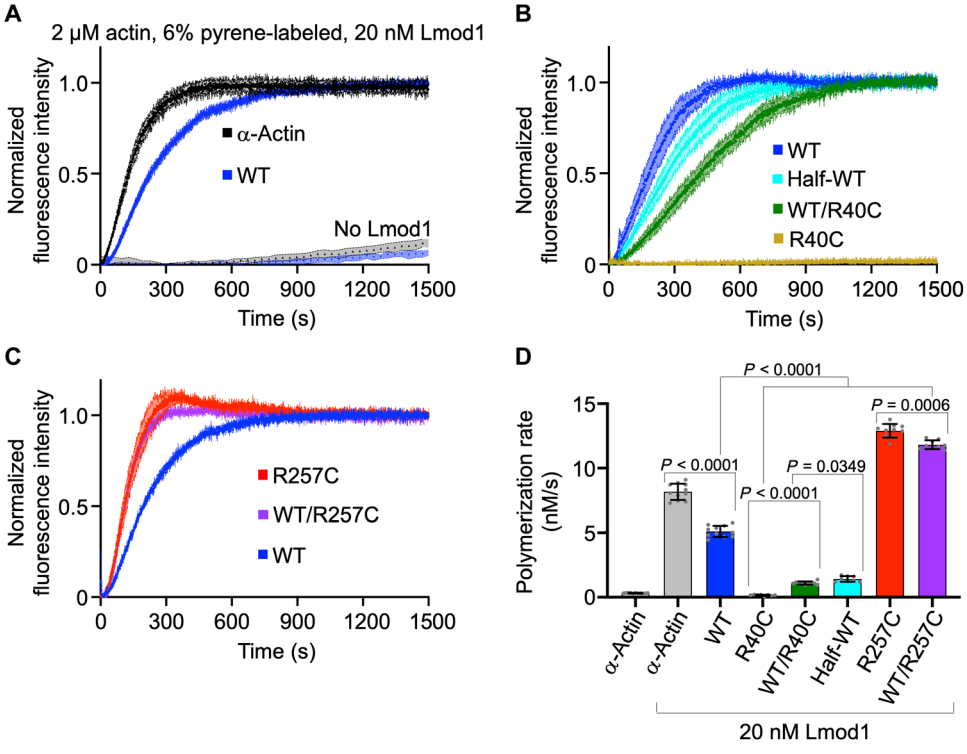

Fig. 3. R40C and R257C affect filament nucleation by Lmod1. (**A** to **C**) Time course of actin polymerization with 20 nM Lmod1 (2 μM total actin, including 6% pyrene-labeled α-actin) showing comparisons between WT ACTG2 and α-actin (A); WT, R40C, WT/R40C, and half-WT (1 μM WT, 12% pyrene-labeled α-actin) (B); and WT, R257C, and WT/R257C (C). (**D**) The polymerization rates of actin variants were calculated from 8 to 11 experiments and at least three independent actin preparations. Data were analyzed by one-way ANOVA with Welch's test ($P < 0.0001$). *P* values are provided from Dunnett's T3 multiple comparisons test. Bar graphs represent means ± SD, with ns indicating *P* values > 0.05.

exhibited extremely slow polymerization with Lmod1, and WT/R40C polymerized slower than half-WT (1 μM WT, 12% pyrene-labeled α-actin) (Fig. 3, B and D, and table S2). This result suggests that, while R40C mostly fails to copolymerize with WT (Fig. 2B), it can be incorporated into the three-actin polymerization nucleus formed by Lmod1 (*18*, *28*, *29*). The resulting "poisoned" nuclei fail to elongate, decreasing the overall polymerization. Last, Lmod1 increased the polymerization rate of R257C and WT/R257C, but the fold increase in both cases was less than for WT, suggesting that R257C interacts inefficiently with Lmod1 (Fig. 3, C and D, and table S2).

R40C and R257C affect filament length but not myosin motility

Some patients with VM have mutations in smooth muscle myosin (*10*, *11*), whose adenosine 5′-triphosphate (ATP)–dependent, cyclical interaction with ACTG2-containing F-actin drives the contraction and relaxation of visceral smooth muscle (*6*). We asked if ACTG2 mutations affected the interaction with smooth muscle myosin and the myosin-dependent motility of F-actin using a gliding assay (*30*). In this assay, we used smooth muscle myosin construct SMM-S1, comprising the motor domain and essential light chain (MYL6). Fluorescent, rhodamine-phalloidin–stabilized actin filaments were applied to SMM-S1–coated coverslips to directly visualize the movement of filaments propelled by myosin heads (Fig. 4).

At time = 0, i.e., immediately after the application of actin filaments onto SMM-S1–coated coverslips, the median filament length was approximately the same for WT ACTG2 and α-actin (Fig. 4, A and B, and table S2). In contrast, despite the stabilizing effect of rhodamine-phalloidin, filaments formed by R40C were significantly shorter than those formed by WT ACTG2. Filaments formed by WT/R40C also appeared shorter than those formed by WT, but this difference was not statistically significant at time = 0. The R257C mutation did not appear to affect the initial median filament length, either alone or when mixed with WT (Fig. 4, A and B, and table S2).

In contrast, despite the stabilizing effect of rhodamine-phalloidin, R257C filaments fragmented when pulled on by SMM-S1 during the time course of the gliding assay (movie S1). This observation prompted us to determine the filament length at four different time points (time = 0, 2, 4, and 6 min). While the median filament length remained relatively stable or increased slightly over time for WT, R40C, and WT/R40C (Fig. 4C), there was a steady decrease in the median filament length for R257C and WT/R257C (Fig. 4, A and D). This result suggests that the R257C mutation renders filaments prone to breakage under the pulling forces of smooth muscle myosin. We further observed that the difference in length between WT and WT/R40C filaments persisted and became statistically significant over time (Fig. 4C), indicating that R40C contributes to polymerization when stabilized by rhodamine-phalloidin.

The filament gliding velocity was similar for α-actin and WT ACTG2 and unaffected by the R40C and R257C mutations (Fig. 4E, movie S1, and table S2). This finding suggests that SMM-S1 does not distinguish between the two actin isoforms and that compromised myosin motility is not the underlying cause of VM for the two ACTG2 mutations analyzed.

Tpm1.4 partially rescues the defects of R40C and R257C

Over 40 tropomyosin (Tpm) isoforms are expressed in humans in a cell-specific and tissue-specific manner (*31*). Tpm isoforms decorate actin filaments to regulate their interactions with ABPs and actomyosin contraction. To investigate the effect of ACTG2 mutations on filament behavior and myosin-driven motility in the presence of Tpm, we performed gliding assays using filaments decorated with Tpm1.4. This Tpm isoform has been found in association with contractile filaments in human smooth muscle cells (*32*, *33*). To preserve the natural N-terminal acetylation-dependent end-to-end interaction of Tpm1.4 coiled coils on F-actin, Tpm1.4 was expressed in human cells for proper posttranslational modification, and the C-terminal affinity tag was precisely removed (*34*). Actin variants labeled with rhodamine-phalloidin were polymerized at a 4:1 ratio with Tpm1.4, and 2 μM Tpm1.4 was added to the final solution to ensure saturation of the filaments (Fig. 5A and movie S2). For most actin variants, the median filament length was 20 to 33% shorter with Tpm1.4 than without (Fig. 5B, fig. S4, and table S2). This effect seems to be due to an increase in the number of shorter filaments visualized as they become more likely to adhere to SMM-S1–coated coverslips when Tpm1.4 is present. The exception was R40C, whose median filament length increased by ~16% in the presence of Tpm1.4, indicating a stabilizing effect of Tpm1.4 (Fig. 5B, fig. S4, and table S2).

For all actin variants analyzed, filament gliding velocities were approximately fourfold faster with Tpm1.4 than without (table S2), which is consistent with previous observations (*35*). However, as observed in the absence of Tpm1.4 (Fig. 4E and table S2), there was no significant difference in gliding velocity among filaments of different actin isoforms, mutants, or WT/mutant mixtures in the presence of Tpm1.4 (Fig. 5C). These results indicate that SMM-S1 does not distinguish between these actin variants with or without Tpm1.4. In addition, Tpm1.4 appeared to protect R257C filaments from breaking under the pulling forces of SMM-S1 as the median length was approximately the same for R257C-Tpm1.4 and WT filaments over time (Fig. 5D).

R40C and R257C impair subunit-subunit contacts in the actin filament

To better understand the effects of the R40C and R257C mutations on filament stability, we obtained high-resolution (2.45 to 2.72 Å) cryo–electron microscopy (cryo-EM) structures of WT ACTG2, R40C, and R257C filaments using helical reconstruction (Fig. 6, fig. S5, and table S3). Nucleotide hydrolysis and γ-phosphate release occurred during sample preparation, before vitrification, resulting in all three structures containing Mg–adenosine 5′-diphosphate-bound actin subunits. The three structures are very similar overall and also similar to that of α-actin (*19*, *20*). No changes in helical twist or rise were observed. Closer inspection, however, reveals how the mutations disrupt inter- and intrasubunit contacts in the filament.

Residue R40 is located within the D-loop of actin, responsible for crucial intersubunit contacts both within and between the two long-pitch helices (or strands) of F-actin (*21*). R40C filaments for cryo-EM analysis could only be obtained in the presence of phalloidin (unlabeled). The absence of the arginine side chain in R40C eliminates contacts observed in the WT structure with the side chain of residue D287 and the main backbone oxygen of G267 (Fig. 6, A and B). These residues belong to two different adjacent subunits: one on the long-pitch helix (D287) and one on the short-pitch helix (G267), making the R40C mutation particularly disruptive to the filament structure. Phalloidin binds near residue R40 and establishes new lateral and longitudinal contacts with the long-pitch helices, explaining how it can partially rescue R40C polymerization in vitro.

In the WT structure, residue R257 forms an important intrasubunit salt bridge with E196, located on a loop that contacts a

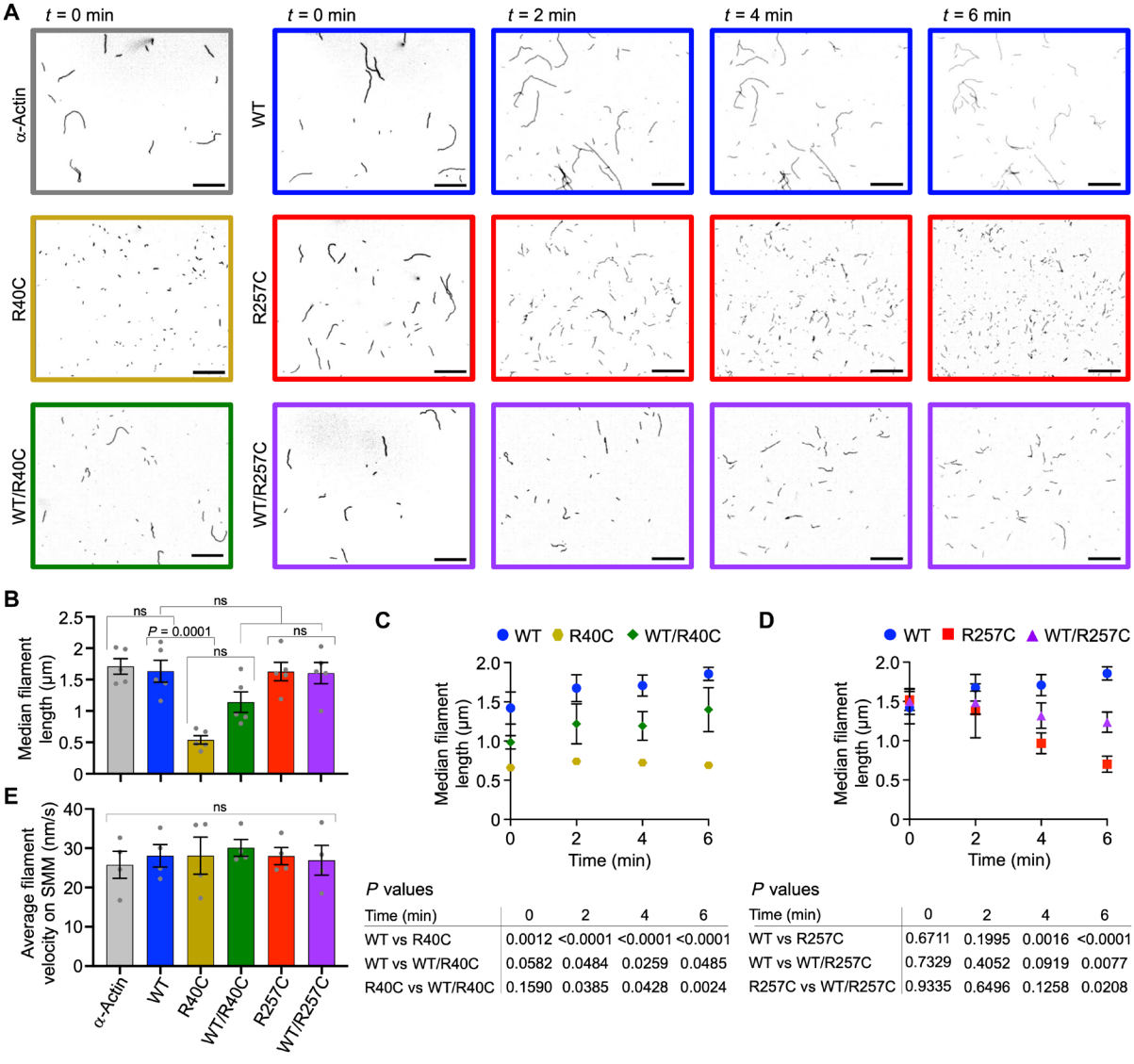

P values

Time (min)	0	2	4	6
WT vs R40C	0.0012	<0.0001	<0.0001	<0.0001
WT vs WT/R40C	0.0582	0.0484	0.0259	0.0485
R40C vs WT/R40C	0.1590	0.0385	0.0428	0.0024

P values

Time (min)	0	2	4	6
WT vs R257C	0.6711	0.1995	0.0016	<0.0001
WT vs WT/R257C	0.7329	0.4052	0.0919	0.0077
R257C vs WT/R257C	0.9335	0.6496	0.1258	0.0208

Fig. 4. Mutants R40C and R257C affect filament length but not myosin motility. (**A**) Representative epifluorescence images of rhodamine-phalloidin α-actin (gray), WT ACTG2 (blue), R40C (gold), R257C (red), WT/R40C (green), and WT/R257C (purple) gliding on SMM-S1–coated coverslips at different times (as indicated; scale bars, 10 μm). (**B**) Filament length quantification at time = 0 ($n = 5$ experiments). (**C** and **D**) Filament length quantification over time for WT, R40C, and WT/R40C (C) and WT, R257C, and WT/R257C (D) ($n = 5$ experiments from at least three independent actin preparations). (**E**) Quantification of SMM-S1–driven filament velocities. Filaments were manually tracked in ImageJ ($n = 4$ experiments). Data in (B) and (E) were analyzed by one-way ANOVA ($P < 0.0001$), with *P* values from Bonferroni's multiple comparisons test. Data from (C) and (D) were analyzed by two-way repeated measures (RM) ANOVA. *P* values, displayed in tables below the graphs, are from Tukey's multiple comparisons test. Data were pooled from three actin and two SMM-S1 independent preparations. Graphs show means ± SEM, with ns indicating *P* values > 0.05.

protomer from the opposite long-pitch helix (Fig. 6, B and C). The R257C mutation abolishes this salt bridge, destabilizing lateral interstrand contacts within the filament. The observed structural effects of the R257C mutation are less severe than those of the R40C mutation. Consistently, R257C polymerizes better than R40C, yet R257C filaments are susceptible to fragmentation when pulled by myosin heads.

DISCUSSION

The six human actin isoforms are highly similar, with sequence identities ranging from 93 to 99% (*15*), yet they play cell-specific and tissue-specific roles and exhibit distinct biochemical properties (*14*, *36*–*40*). In this context, our findings reveal that WT ACTG2, which is primarily expressed in the smooth muscle of hollow organs, behaves as a less dynamic isoform compared to α-actin. It exhibits slower polymerization and depolymerization rates than α-actin, along with a higher Cc for polymerization (Fig. 2, A and D to H, and table S2). WT ACTG2 also polymerizes at a slower rate than α-actin in the presence of the smooth muscle actin filament nucleator Lmod1. Yet, the fold change in the polymerization rate with and without Lmod1 is approximately the same for both isoforms (Fig. 3, A and D, and table S2). There is also no significant difference in the SMM-S1–driven gliding velocity of filaments formed by WT

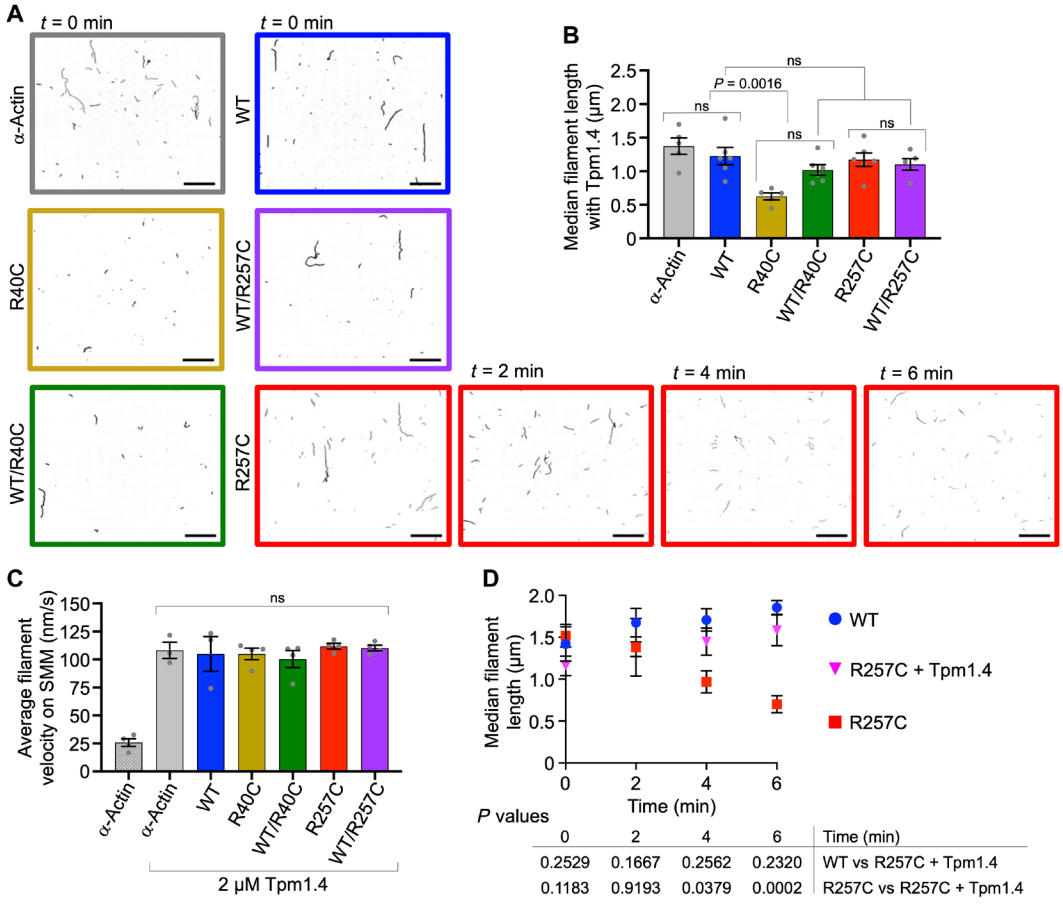

Fig. 5. Tpm1.4 partially rescues the defects of R40C and R257C. (**A**) Representative epifluorescence images of Tpm1.4-coated rhodamine-phalloidin α-actin (gray), WT ACTG2 (blue), R40C (gold), R257C (red), WT/R40C (green), and WT/R257C (purple) gliding on SMM-S1–coated coverslips at different times (as indicated; scale bars, 10 μm). (**B**) Filament length quantification with Tpm1.4 at time = 0 ($n = 5$ to 6 experiments). Data were analyzed by one-way ANOVA ($P = 0.0007$), and P values are from Bonferroni's multiple comparisons test. (**C**) Quantification of SMM-S1–driven filament velocities. Filaments were manually tracked in ImageJ ($n = 4$ experiments). Quantification of filament velocity ($n = 4$ experiments). Data were analyzed by one-way ANOVA with Welch's ANOVA tests ($P = 0.7873$), and P values are from Dunnett's T3 multiple comparisons test. (**D**) Filament length quantification over time for WT, R257C, and R257C + Tpm1.4 ($n = 5$ experiments). Data were analyzed by two-way RM ANOVA. P values, displayed in the table below the graph, are from Tukey's multiple comparisons test. Data were pooled from three actin and two SMM-S1 independent preparations. Graphs display means ± SEM, with ns indicating P values > 0.05.

0	2	4	6	Time (min)
0.2529	0.1667	0.2562	0.2320	WT vs R257C + Tpm1.4
0.1183	0.9193	0.0379	0.0002	R257C vs R257C + Tpm1.4

ACTG2 and α-actin, with or without Tpm1.4 (Figs. 4E and 5C). These observations suggest that Lmod1, smooth muscle myosin, and Tpm1.4 do not discriminate between these two isoforms. More likely, it is the cumulative effect of minor differences, such as those observed here, that define the tissue specificity of actin isoforms. In addition, in their respective tissues, ACTG2 and α-actin associate with tissue-specific Tpm isoforms, providing an additional layer of regulation and differentiation of their actin-Tpm copolymers (*41*).

The four disease-causing mutations studied here disrupt ACTG2 function in distinct ways, affecting the stability of G-actin or F-actin, altering the polymerization kinetics, or disrupting interactions with ABPs and actin itself within the filament. As discussed below, the observed biochemical and structural disruptions of the mutants appear to correlate with the range of disease severity observed in patients with VM.

ACTG2 R148C

The biochemical analysis of mutations of actin residue R148, including R148C, has proven challenging. An attempt to purify the equivalent mutation in smooth muscle α-actin (ACTA2 R149C) from Sf9 cells was unsuccessful due to this mutant's association with the chaperonin complex (*42*). Chaperonin complex association did not pose a problem in our study, which used human cell expression. However, while the expression of ACTG2 R148C was robust, its purification was also limiting here due to poor binding of the mutant to the Ca^{2+}-dependent G4G6 affinity column (Fig. 1C and fig. S2B) (*14*). The inefficient binding of R148C to G4G6 is nonetheless revealing of the relatively mild disease phenotype of this mutation. In cells, multiple families of ABPs orchestrate the assembly and disassembly of actin filaments (*26*). Most of these ABPs, including gelsolin (*25*), interact with the hydrophobic cleft in actin, which also mediates intersubunit contacts in the filament (*21*, *22*). R148C and other mutations within this cleft are likely to disrupt these interactions and thus be excluded from filaments due to their inability to bind filament assembly factors such as formins and WH2-domain containing proteins that also target this cleft (*43*). Supporting this view, tagged R148 mutants overexpressed in immortalized cell lines show reduced colocalization with phalloidin-stained filament structures

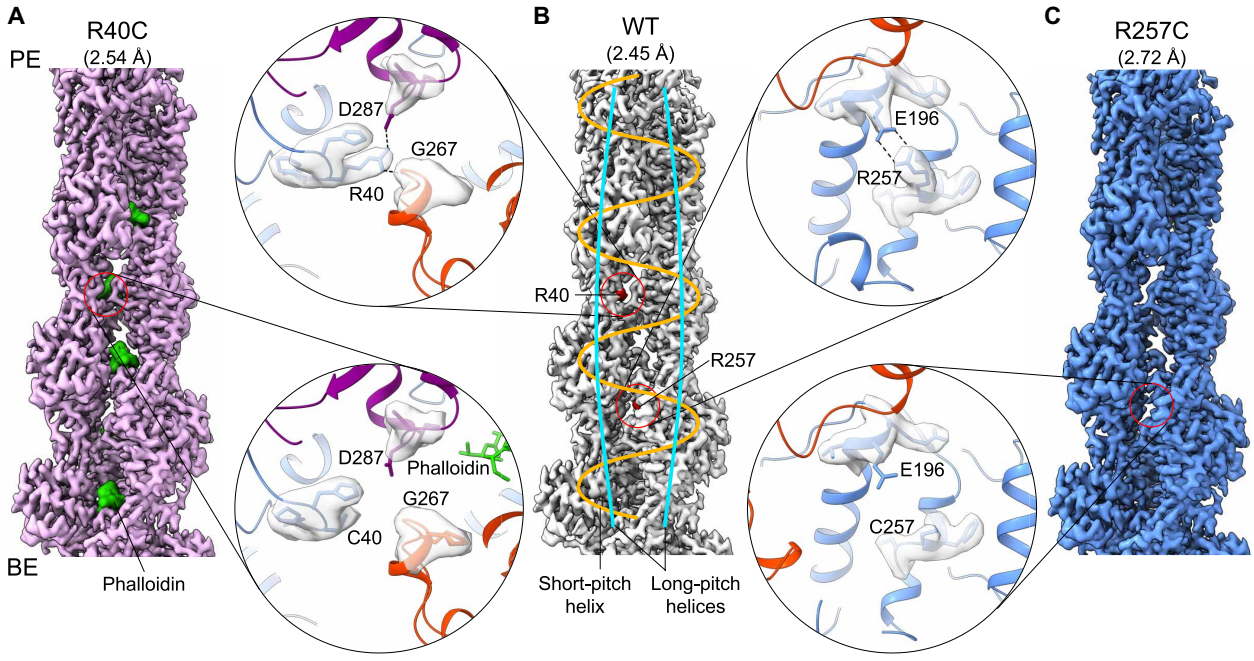

Fig. 6. R40C and R257C impair subunit-subunit contacts in F-actin. (**A** to **C**) Cryo-EM maps of R40C (purple), WT (gray), and R257C (blue) with resolutions of 2.54, 2.45, and 2.72 Å, respectively. The polymerization of R40C is inefficient, requiring its structure to be determined with bound phalloidin (green). Close-up ribbon diagrams highlighting local differences between WT and the mutants and the disruption of inter- and intrasubunit contacts (dashed lines). Different actin subunits in the vicinity of the mutations are colored differently. The definition of the short-pitch (orange) and long-pitch (cyan) helices is shown on the WT map. PE and BE indicate pointed and barbed ends, respectively.

(*44*, *45*). Moreover, large actin-positive aggregates form in the smooth muscle cells of patients with VM carrying R148 mutations (*24*, *44*). These observations are consistent with R148 variants being excluded from filaments and accumulating in cells, leading to disruption of the smooth muscle cell architecture and contractility.

ACTG2 R178C

The R178C mutation is associated with the most severe VM presentation, MMIHS, and overexpression of mutants of residue R178 in cell cultures leads to more severe contractility defects than other ACTG2 mutants (*4*, *45*, *46*). In addition, mutations of the corresponding amino acid in ACTA2 (R179) cause multisystem smooth muscle dysfunction syndrome, a condition affecting both visceral and vascular smooth muscle (*47*). While ACTG2 R178C was successfully purified, reliable biochemical data could not be obtained due to protein degradation during dialysis. This contrasts with WT, R40C, R148C, and R257C, which were all proteolytically stable after purification (Fig. 1C and fig. S2, C and D). Other than its tendency to degrade, R178C also failed to polymerize, precluding further analysis and consistent with protein misfolding. A prior analysis of ACTA2 R179H also reported severe polymerization defects, albeit not protein degradation (*39*). The degradation of ACTG2 R178C observed here may possibly result from the more severe impact on protein stability of an arginine mutation to cysteine than histidine. R178 makes important contacts between the two major actin domains, which rotate relative to one another during the G-actin to F-actin transition (*20*, *48*). By disrupting this important linkage, the R178C mutation may allow the domains to move uncoordinatedly and expose the hydrophobic core of the actin monomer. R178C might also be misfolded in cells, which could compromise smooth muscle contractility through activation of the unfolded protein response pathway (*49*).

ACTG2 R40C

Mutations of ACTG2 residue R40 cause pediatric-onset VM, with associated defects extending to the bladder (*4*). While R40C expressed and purified successfully, this mutation severely impaired polymerization both alone or stimulated by Lmod1 (Fig. 1C; Fig. 2, B and D; Fig. 3, B and D; and table S2). The inefficient polymerization of R40C impeded a reliable estimation of its polymerization and depolymerization rates and Cc for filament assembly. Nevertheless, short R40C filaments were obtained with the addition of phalloidin, enabling analyses of this mutant's structure and filament gliding velocity by myosin, with or without Tpm1.4 (Fig. 4, A and E; Fig. 5, A and C; and table S2). R40C is situated within the D-loop in actin, which mediates important intersubunit contacts within F-actin by inserting into the hydrophobic cleft of the long-pitch subunit immediately above (*21*). As observed in the structure (Fig. 6, A and B), the R40C mutation falls near the binding site of phalloidin and breaks important intersubunit contacts both within and between the two long-pitch helices of the filament. These observations explain both the disruptive effect of the mutation on polymerization and the stabilizing effect of phalloidin on filament formation by R40C.

In contrast, the R40C mutation falls farther away from the binding surfaces of myosin and Tpm (fig. S6) (*23*), whose interactions with R40C filaments remained unaffected (Figs. 4E and 5C). For most actin variants studied here, the median filament length decreased slightly in the presence Tpm1.4 (fig. S4 and table S2). We suggest that this effect is due to a greater number of smaller filaments

appearing within the field of view as a result of filaments binding more avidly to myosin heads on the coverslip when decorated with Tpm1.4 (*50*). Despite this general effect, the addition of Tpm1.4 slightly increased the median length of R40C filaments (fig. S4 and table S2). Tpm forms a rope-like polymer on each side of F-actin, which appears to add to the stabilizing effect of phalloidin on R40C filaments.

Because most VM-causing ACTG2 mutations are heterozygous, coexisting with WT in cells (*1*), we also studied 50/50 mixtures of WT and mutants. This analysis revealed that R40C mostly does not copolymerize with WT as the WT/R40C mixture polymerized at approximately the same rate as half-WT, had a twofold lower Cc, and depolymerized at a similar rate as WT (Fig. 2, B, D, F, and H; fig. S3, C and E; and table S2). However, WT/R40C hindered nucleation by Lmod1, showing slower polymerization than half-WT (Fig. 3, B and D, and table S2). This result suggests that R40C can be incorporated as a subunit into the three-actin polymerization nucleus formed by Lmod1 (*18*). However, R40C's incorporation into the Lmod1-formed nucleus inhibits elongation, which is independent of Lmod1, thus exerting a dominant negative effect on the polymerization rate of WT in the mixture.

Myosin glided all the F-actin species analyzed here (α-actin, WT, R40C, R257C, and their 50/50 mixtures with WT) with similar velocities, and approximately fourfold faster when filaments were decorated with Tpm1.4 (Figs. 4E and 5C). That myosin and Tpm1.4 do not discriminate between these filaments is not unexpected; α-actin and ACTG2 share 98.4% sequence identity, and the mutations R40C and R257C do not affect the binding surfaces of Tpm nor myosin (fig. S6) (*23*). Collectively, our observations suggest that R40C is likely to cause disease through its markedly compromised polymerization. Our findings are consistent with a previous cellular study that showed reduced incorporation of ACTG2 R40C into filaments (*45*), potentially indicating that this mutant exists mostly as G-actin and may sequester ABPs, like Lmod1, that are necessary for muscle function.

ACTG2 R257C

R257C, the most frequently observed VM mutation, is associated with severe pediatric-onset disease that commonly affects the bowel and bladder function (*4*). Unexpectedly, R257C polymerized and depolymerized faster and exhibited a lower Cc than WT ACTG2 (Fig. 2, C, D, F, and H; fig. S3, D and F; and table S2). Lmod1 enhanced R257C polymerization, albeit to a lesser extent compared to WT (Fig. 3, C and D, and table S2), which might be attributed to compromised Lmod1 binding or masking of the stimulatory effect of Lmod1 due to the mutant's intrinsically faster polymerization rate. WT and R257C appear to copolymerize since their 50/50 mixture displays values of polymerization, Cc, and Lmod1-driven polymerization intermediate between those of the mutant and WT (Fig. 2, C, D, and H; Fig. 3, C and D; fig. S3F; and table S2).

While the initial median length and gliding velocity of R257C and WT filaments were similar (Fig. 4, B and E), myosin fragmented R257C and WT/R257C filaments over time, suggesting a destabilizing effect of the mutation on actin filament structure (Fig. 4D). This observation is consistent with the cryo-EM structure, which revealed that the R257C mutation removes intra- and intersubunit contacts at the interface between the two long-pitch helices and away from the myosin- and Tpm-binding surfaces (Fig. 6, B and C, and fig. S6). As with R40C, Tpm1.4 had a stabilizing effect on R257C filaments, inhibiting fragmentation (Fig. 5D). The susceptibility of R257C filaments to fragmentation likely explains the faster polymerization and depolymerization rates observed with this mutant. Fragmentation generates new barbed and pointed ends that gain and lose subunits in polymerization and depolymerization reactions, respectively. This effect is somewhat analogous to the increase or decrease in polymerization resulting from filament severing by cofilin as a function of the monomer concentration (*51*, *52*). At high monomer concentrations, barbed ends generated by cofilin elongate, whereas below the Cc, the ends depolymerize. We note that the forces exerted on filaments in gliding assays are substantially lower than those produced by cell and tissue contraction. Therefore, in cells and tissues, filament fragmentation with mutant R257C may occur even in the presence of Tpm, adding to this mutant's dysfunction in VM. Overall, our results suggest lower stability of R257C filaments, potentially explaining the increased G- to F-actin ratio observed in cells expressing this mutant (*53*, *54*).

Comparisons with the corresponding mutation in ACTA2 (R258C) that causes familial thoracic aortic aneurysms and dissection reveal discrepancies. Unlike our findings, ACTA2 R258C polymerized more slowly and had a higher Cc than WT ACTA2 by total internal reflection fluorescence microscopy (*55*). Moreover, filament fragmentation was not observed in gliding assays, and Tpm appeared to hinder myosin binding to ACTA2 R258C filaments, contrasting with our observed roughly fourfold increase in gliding velocity with Tpm1.4-decorated ACTG2 R257C filaments. Because the two smooth muscle actin isoforms differ only by four amino acids, these differences may stem from variations in the expression and purification methods used in the two studies (*14*).

In summary, the most common ACTG2 mutations linked to VM disrupt smooth muscle function via different biochemical mechanisms: R40C disrupts actin polymerization, R148C perturbs interactions with ABPs, R178C affects protein folding leading to aggregation and degradation, and R257C destabilizes filaments such that they become prone to fragmentation under tension. This knowledge can inform the behavior of related ACTG2 mutations and aid the development of mechanism-based therapies for VM.

MATERIALS AND METHODS

Proteins

Mutants (R40C, R148C, R178C, and R257C) of human ACTG2 (UniProt P63267) were created using the QuikChange II XL mutagenesis kit (Agilent Technologies) with primers listed in table S4. WT and mutant ACTG2 variants were expressed and purified as we recently described (*14*), using a His-FLAG-TEV-ACTG2 construct and FLAG-dependent and Ca^{2+}-dependent gelsolin G4G6 affinity columns. Briefly, proteins were expressed in Expi293F cells (Thermo Fisher Scientific) at 37°C with 8% CO_2 for 48 hours, and cells were harvested and stored at −80°C. Cell pellets were thawed and lysed in a Dounce homogenizer with 25 mM sucrose-containing lysis buffer [10 mM Tris-HCl (pH 8), 10 mM $CaCl_2$, 2 mM $MgCl_2$, 0.1% octyl-β-glucoside, and 0.5 mM ATP] and protease inhibitors. The lysate, after centrifugation, was incubated overnight at 4°C with recombinant His-G4G6, loaded onto an anti-FLAG column (GenScript Biotech) and eluted with low pH buffer (100 mM glycine, pH 3.5) directly into a neutralizing buffer [100 mM Tris-HCl (pH 8), 10 mM $CaCl_2$, 1 mM $MgCl_2$, and 0.5 mM ATP]. Elution fractions were incubated with His-TEV protease to remove the N-terminal affinity tag

from ACTG2 and His-Naa80Δ (residues 78 to 308, with acetyl coenzyme A) to acetylate the N terminus (*16*) during overnight dialysis in G-buffer [5 mM Tris-HCl (pH 8), 0.2 mM $CaCl_2$, 0.2 mM ATP, and 0.1 mM NaN_3] at 4°C. His-MBP-G4G6 was added before loading onto a Ni-NTA column (Thermo Fisher Scientific). After extensive washing, ACTG2 was eluted in 10 mM Tris-HCl (pH 8), 1 mM $MgCl_2$, and 0.5 mM ATP with the addition of 3 mM EGTA that dissociates ACTG2 from G4G6 while His-MBP-G4G6, His-TEV, His-Naa80Δ, and any uncut His-FLAG-TEV-ACTG2 remain on the column. All the ACTG2 variants were produced in parallel, dialyzed into G-buffer overnight at 4°C, and polymerized (except R40C) and depolymerized before analysis. Proteins underwent centrifugation at 200,000*g* for 30 min, and their concentrations were determined spectrophotometrically using ε (λ = 290 nm) = 266,000 M^{-1} cm^{-1}. Protein yields ranged from 0.2 to 0.5 mg per liter of culture, which is lower than what we previously obtained for skeletal α-actin and cytoplasmic β-actin (*14*).

α-Actin was purified from rabbit skeletal muscle (Pel-Freez Biologicals) (*56*). For polymerization/depolymerization assays, α-actin was labeled with *N*-(1-pyrene)iodoacetamide (Toronto Research Chemicals), referred to here as pyrene-labeled α-actin.

Recombinant baculovirus carrying a C-terminally FLAG-tagged and Myc-tagged SMM-S1 construct (provided by L. Sweeney) was coexpressed with a virus encoding the essential light chain (MYL6) in Sf9 cells (*57*). The cell pellet was washed, rapidly frozen, and stored at −80°C. For purification, the pellet was lysed with a Dounce homogenizer in 10 mM Tris-HCl (pH 7.5), 200 mM NaCl, 4 mM $MgCl_2$, 1 mM EGTA, 0.5% IGEPAL,1 mM β-mercaptoethanol (βME), 1 mM dithiothreitol (DTT), and protease inhibitors. Lysed cells were clarified by centrifugation at 162,000*g* for 1 hour. The supernatant was loaded onto a 2-ml anti-FLAG column and washed with 10 mM Tris-HCl (pH 7.5), 200 mM NaCl, 4 mM $MgCl_2$, 1 mM EGTA, 1 mM βME, 1 mM DTT, and protease inhibitors. SMM-S1 was eluted after 90-min incubation with 10 mM Tris-HCl (pH 7.5), 200 mM NaCl, 1 mM EGTA, 1 mM DTT, FLAG peptide (0.2 mg/ml), and protease inhibitors. The protein was further purified on a Mono Q column with a 50 to 1000 mM KCl gradient in 10 mM Tris-HCl (pH 7.5), 1 mM EGTA, and 1 mM DTT (SMM-S1 elutes at ~600 mM KCl). Purified SMM-S1 was dialyzed overnight at 4°C in 60 mM Mops (pH 7.0), 100 mM KCl, 1 mM EGTA, 1 mM $MgCl_2$, 1 mM DTT, and 50% glycerol, aliquoted, and stored at −20°C. The protein concentration was determined using the Bradford colorimetric assay (Bio-Rad) and bovine serum albumin (BSA) standards (Thermo Fisher Scientific). Before use, SMM-S1 was mixed with phalloidin-stabilized actin filaments in the presence of 2 mM $MgCl_2$ and 2 mM ATP, followed by centrifugation at 200,000*g* for 1 hour to remove inactive myosin heads.

The human Lmod1 protein used in this study was previously obtained and stored at −80°C (*18*). Upon thawing, the activity of the sample was verified through polymerization assays with pyrene-labeled α-actin.

Human Tpm1.4 was cloned and purified as we have described previously (*34*). Briefly, Tpm1.4-Intein-CBD was expressed in Expi293F cells at 37°C with 8% CO_2 for 48 hours. Cells were lysed with a Dounce homogenizer, and the protein was purified using a chitin affinity column (New England Biolabs). Intein cleavage was induced overnight with 40 mM DTT at room temperature. Tpm1.4 was further purified through a Mono Q column, concentrated, and stored at −80°C.

Antibodies

The commercial antibodies used in this study are listed in table S5 and were used following the instructions of the manufacturer.

Pyrene-actin polymerization

Actin polymerization was measured as the time course of the fluorescence increase resulting from pyrene-actin incorporation into filaments in experiments conducted at 25°C. Polymerization of actin alone was performed using a Cytation 5 imaging plate reader (BioTek), while polymerization in the presence of 20 nM Lmod1 was conducted on a Cary Eclipse fluorescence spectrophotometer (Varian Medical Systems). Before data acquisition, 4 μl of G-buffer or 4 μl of Lmod1 was added to 196 μl of 2 μM Mg-ATP-actin variants (including 6% pyrene-labeled α-actin) in F-buffer [10 mM Tris-HCl (pH 8), 1 mM $MgCl_2$, 50 mM KCl, 1 mM EGTA, 0.2 mM ATP, 0.5 mM DTT, and 0.1 mM NaN_3]. Polymerization curves were normalized by dividing each point by the total fluorescence increase. Polymerization rates are reported as the maximum slopes of the polymerization curves, divided by the total change in fluorescence at the polymerization plateau, and multiplied by 2 μM minus the measured Cc for each actin variant. For R40C, the polymerization rate was estimated based on WT ACTG2 parameters.

Pyrene-actin depolymerization

Actin depolymerization reactions were conducted as described previously (*58*). Briefly, 4 μM actin variants (including 10% pyrene-labeled α-actin) were polymerized in F-buffer for 4 hours at 25°C. Before data acquisition, polymerized actin was diluted below the Cc (0.1 μM in 200 μl) in G-buffer with 0.2 mM $MgCl_2$ (instead of 0.2 mM $CaCl_2$) to induce depolymerization. Depolymerization curves were recorded with a Cytation 5 imaging plate reader, and the data were fitted by two-phase exponential decay in GraphPad Prism (version 10.0.3) in which the fast rate constant corresponds to the depolymerization rate for each experiment. Each actin variant was analyzed concurrently with α-actin (control), and depolymerization rates were normalized to the rate of α-actin. Non-normalized depolymerization rates are also reported in table S2.

Cc measurements

Pyrene fluorescence at equilibrium was measured following overnight incubation of different concentrations of actin variants (including 5% pyrene-labeled α-actin) in F-buffer. For each concentration, control reactions were recorded with 5% pyrene-labeled α-actin alone (i.e., added to F-buffer). The change in fluorescence was determined by subtracting the pyrene-labeled α-actin control from the corresponding equilibrium fluorescence measurements of each actin variant and plotted against the actin concentration. The Cc (*x* intercept) was calculated from the linear trend line using Microsoft Excel. For each actin variant, the Cc is reported as the mean from three independent experiments.

Gliding assays

Actin (4 μM ACTG2 variants or 2 μM α-actin) was polymerized for 2 hours at room temperature in 60 mM Mops (pH 7.0), 25 mM KCl, 1 mM $MgCl_2$, 1 mM EGTA, and 1 mM DTT, and filaments were stabilized with rhodamine-phalloidin (Invitrogen). In experiments involving Tpm1.4, actin was copolymerized with 1 μM Tpm1.4 (0.5 μM Tpm1.4 for α-actin), and an additional 2 μM Tpm1.4 was added to the final assay solution flowed into the chamber. Gliding assays

were performed on 0.5% nitrocellulose-coated coverslips (collodion 2% in amyl acetate, Electron Microscopy Sciences). Reagents were added to the chamber in the following order: c-Myc antibody (0.1 mg/ml; Developmental Studies Hybridoma Bank), BSA (2 mg/ml; Sigma-Aldrich), 25 µl of 3.5 to 5 µM Myc-tagged SMM-S1 incubated for 5 min (x3), and 75-µl wash with BSA (2 mg/ml). The final assay solution contained 10 nM rhodamine-phalloidin–stabilized actin filaments (20 nM for the WT/R40C mixture), 0.1% methylcellulose, 2 mM $MgCl_2$, 2 mM ATP, glucose (5 mg/ml), glucose oxidase (92 U/ml; Sigma-Aldrich), bovine liver catalase (48 mg/ml; Roche), and BSA to prevent nonspecific binding. Motility chambers were sealed with vacuum grease. Fluorescent actin filaments were visualized using a Leica DMIRB microscope with a 100-fold magnification Leica oil-immersion objective (aperture 1.4). An initial image was taken within seconds of chamber sealing, and video acquisition started after 2-min incubation on the objective heater to equilibrate the temperature at 30°C. Actin filament lengths were manually measured in ImageJ (https://imagej.net/ij/), using 20 to 80 filaments per image, depending on the filament density. For velocity measurements, the leading end of 8 to 12 filaments per video were tracked using the Manual Tracking plugin of ImageJ, and the average velocities were calculated from the displacement over time using Microsoft Excel. Filament length over time was assessed by manually measuring 25 to 60 filaments at each time point from each video (movies S1 and S2). Data for each condition were pooled from at least three actin and two SMM-S1 preparations.

Cryo-EM analysis

Actin (4 µM) was polymerized in F-buffer for 2 hours at room temperature. For R40C, 5 µM phalloidin (Cayman Chemical) was added during polymerization. Samples (3 µl) were applied to glow-discharged (90 s; easiGlow, PELCO) R1.2/1.3 200-mesh Quantifoil holey carbon grids (Electron Microscopy Sciences). Grids were blotted for 2.5 s with force 0 using Whatman 41 filter paper and flash-frozen in liquid ethane using a Vitrobot Mark IV (Thermo Fisher Scientific).

Cryo-EM datasets were collected using the EPU software (Thermo Fisher Scientific) on a 300-keV FEI Titan Krios transmission electron microscope equipped with a Gatan K3 direct electron detector and an energy filter (BioQuantum). The number of micrographs collected were 512, 4461, and 1021 for WT, R40C and R257C, respectively. Micrographs were collected at a defocus range of −0.5 to 2.5 µm, with a nominal magnification of ×81,000 and a pixel size of 0.54 Å.

Movies were imported into CryoSPARC v4.0 (*59*) and binned by two during patch motion correction. After patch contrast transfer function (CTF) estimation, actin filaments were manually picked to generate templates. Templates were used to pick filament segments using the filament tracer function of CryoSPARC with a diameter of 90 Å and a 0.3 x diameter increment between segments. Segments (479624, WT; 3423214, R40C; and 493435, R257C) were extracted using a box size of 256 pixels. The best particles (or segments) were selected after two-dimensional (2D) classification (475334, WT; 3400116, R40C; and 380452, R257C) and used in helical refinement and initial map generation.

Initial helical parameters were set to −166° twist and 27.5-Å rise, remaining mostly unchanged during helical refinement. Final particle stacks underwent global and local CTF refinement, followed by additional helical refinement to yield final cryo-EM maps at resolutions of 2.45, 2.54, and 2.72 Å for WT, R40C, and R257C, respectively. The orientation distribution and efficiency of the particle stacks were determined using cryoEF (*60*). The 3D Fourier shell correlation and sphericity of each map were calculated using the 3DFSC server (*61*). Local resolution estimation was done in CryoSPARC. Coot (*62*) and Phenix (*63*) were used for model building and refinement, starting from a high-resolution structure of the filament (PDB code: 8F8P) (*20*). Figures were prepared in ChimeraX (*64*). The cryo-EM workflow and structure quality validation are shown in fig. S5.

Statistical analyses

All statistical analyses were carried out using GraphPad Prism version 10.0.3. Shapiro-Wilk tests were used to validate the normal distribution of datasets. For datasets with $n > 3$, Bartlett's test was used to assess if the SDs differed significantly, guiding the choice between parametric or nonparametric tests. One-way ANOVA tests were used for most experiments with preselected multiple comparisons, and specific test names and results are provided in the figure legends. Two-way ANOVA tests were used for measurements of filament length over time, and the corresponding *P* values are given in the figures. A comprehensive list of statistical tests and *P* values is included in table S6.

Supplementary Materials

This PDF file includes:

Figs. S1 to S6
Tables S1 to S6
Legends for movies S1 and S2
Legend for source data file
References

Other Supplementary Material for this manuscript includes the following:

Movies S1 and S2
Source data file

REFERENCES AND NOTES

1. S. K. Hashmi, R. H. Ceron, R. O. Heuckeroth, Visceral myopathy: Clinical syndromes, genetics, pathophysiology, and fall of the cytoskeleton. *Am. J. Physiol. Gastrointest. Liver Physiol.* **320**, G919–G935 (2021).
2. H. Soh, M. Fukuzawa, A. Kubota, H. Kawahara, T. Ueno, T. Taguchi, Megacystis microcolon intestinal hypoperistalsis syndrome: A report of a nationwide survey in Japan. *J. Pediatr. Surg.* **50**, 2048–2050 (2015).
3. P. Tang, L. Lu, W. Yan, Y. Tao, H. Feng, W. Cai, Y. Wang, Long-term follow-up for pediatric intestinal pseudo-obstruction patients in China. *Nutr. Clin. Pract.* **38**, 648–656 (2023).
4. N. A. Batzir, P. K. Bhagwat, A. Larson, Z. C. Akdemir, M. Baglaj, L. Bofferding, K. B. Bosanko, S. Bouassida, B. Callewaert, A. Cannon, Y. E. Colon, A. D. Garnica, M. H. Harr, S. Heck, A. C. E. Hurst, S. N. Jhangiani, B. Isidor, R. O. Littlejohn, P. Liu, P. Magoulas, H. M. Fan, R. Marom, S. McLean, M. M. Nezarati, K. M. Nugent, M. B. Petersen, M. L. Rocha, E. Roeder, R. Smigiel, I. Tully, J. Weisfeld-Adams, K. O. Wells; Baylor-Hopkins Center for Mendelian Genomics, J. E. Posey, J. R. Lupski, A. L. Beaudet, M. F. Wangler, Recurrent arginine substitutions in the ACTG2 gene are the primary driver of disease burden and severity in visceral myopathy. *Hum. Mutat.* **41**, 641–654 (2020).
5. R. M. Geraghty, S. Orr, E. Olinger, R. Neatu, M. Barroso-Gil, H. Mabillard; Genomics England Research Consortium, I. Wilson, J. A. Sayer, Use of whole genome sequencing to determine the genetic basis of visceral myopathies including Prune Belly syndrome. *J. Rare Dis.* **2**, 9 (2023).
6. H. Lee Sweeney, D. W. Hammers, Muscle contraction. *Cold Spring Harb. Perspect. Biol.* **10**, a023200 (2018).
7. M. F. Wangler, C. Gonzaga-Jauregui, T. Gambin, S. Penney, T. Moss, A. Chopra, F. J. Probst, F. Xia, Y. Yang, S. Werlin, I. Eglite, L. Kornejeva, C. A. Bacino, D. Baldridge, J. Neul, E. L. Lehman, A. Larson, J. Beuten, D. M. Muzny, S. Jhangiani; Baylor-Hopkins Center for Mendelian Genomics, R. A. Gibbs, J. R. Lupski, A. Beaudet, Heterozygous de novo and inherited mutations in the smooth muscle actin (ACTG2) gene underlie megacystis-microcolon-intestinal hypoperistalsis syndrome. *PLOS Genet.* **10**, e1004258 (2014).

8. I. Matera, D. Bordo, M. Di Duca, M. Lerone, G. Santamaria, M. Pongiglione, A. Lezo, A. Diamanti, M. I. Spagnuolo, A. Pini Prato, D. Alberti, G. Mattioli, P. Gandullia, I. Ceccherini, Novel ACTG2 variants disclose allelic heterogeneity and bi-allelic inheritance in pediatric chronic intestinal pseudo-obstruction. *Clin. Genet.* **99**, 430–436 (2021).
9. D. Halim, M. P. Wilson, D. Oliver, E. Brosens, J. B. Verheij, Y. Han, V. Nanda, Q. Lyu, M. Doukas, H. Stoop, R. W. Brouwer, W. F. J. van IJcken, O. J. Slivano, A. J. Burns, C. K. Christie, K. L. de Mesy Bentley, A. S. Brooks, D. Tibboel, S. Xu, Z. G. Jin, T. Djuwantono, W. Yan, M. M. Alves, R. M. Hofstra, J. M. Miano, Loss of LMOD1 impairs smooth muscle cytocontractility and causes megacystis microcolon intestinal hypoperistalsis syndrome in humans and mice. *Proc. Natl. Acad. Sci. U.S.A.* **114**, E2739–E2747 (2017).
10. J. Gauthier, B. O. A. Bencheikh, F. F. Hamdan, S. M. Harrison, L. A. Baker, F. Couture, I. Thiffault, R. Ouazzani, M. E. Samuels, G. A. Mitchell, G. A. Rouleau, J. L. Michaud, J. F. Soucy, A homozygous loss-of-function variant in MYH11 in a case with megacystis-microcolon-intestinal hypoperistalsis syndrome. *Eur. J. Hum. Genet.* **23**, 1266–1268 (2015).
11. C. A. Moreno, N. Sobreira, E. Pugh, P. Zhang, G. Steel, F. R. Torres, D. P. Cavalcanti, Homozygous deletion in MYL9 expands the molecular basis of megacystis-microcolon-intestinal hypoperistalsis syndrome. *Eur. J. Hum. Genet.* **26**, 669–675 (2018).
12. D. Halim, E. Brosens, F. Muller, M. F. Wangler, A. L. Beaudet, J. R. Lupski, Z. H. C. Akdemir, M. Doukas, H. J. Stoop, B. M. de Graaf, R. W. W. Brouwer, W. F. J. van Ijcken, J. F. Oury, J. Rosenblatt, A. J. Burns, D. Tibboel, R. M. W. Hofstra, M. M. Alves, Loss-of-function variants in MYLK cause recessive megacystis microcolon intestinal hypoperistalsis syndrome. *Am. J. Hum. Genet.* **101**, 123–129 (2017).
13. H. Sogawa, G. Costa, S. Armanyous, G. J. Bond, R. J. Cruz, A. Humar, G. Mazariegos, K. M. Abu-Elmagd, Twenty years of gut transplantation for chronic intestinal pseudo-obstruction: Technical innovation, long-term outcome, quality of life, and disease recurrence. *Ann. Surg.* **273**, 325–333 (2021).
14. R. H. Ceron, P. J. Carman, G. Rebowski, M. Boczkowska, R. O. Heuckeroth, R. Dominguez, A solution to the long-standing problem of actin expression and purification. *Proc. Natl. Acad. Sci. U.S.A.* **119**, e2209150119 (2022).
15. T. Arnesen, R. Marmorstein, R. Dominguez, Actin's N-terminal acetyltransferase uncovered. *Cytoskeleton* **75**, 318–322 (2018).
16. G. Rebowski, M. Boczkowska, A. Drazic, R. Ree, M. Goris, T. Arnesen, R. Dominguez, Mechanism of actin N-terminal acetylation. *Sci. Adv.* **6**, eaay8793 (2020).
17. J. N. Rao, Y. Madasu, R. Dominguez, Mechanism of actin filament pointed-end capping by tropomodulin. *Science* **345**, 463–467 (2014).
18. M. Boczkowska, G. Rebowski, E. Kremneva, P. Lappalainen, R. Dominguez, How Leiomodin and Tropomodulin use a common fold for different actin assembly functions. *Nat. Commun.* **6**, 8314 (2015).
19. W. Oosterheert, B. U. Klink, A. Belyy, S. Pospich, S. Raunser, Structural basis of actin filament assembly and aging. *Nature* **611**, 374–379 (2022).
20. P. J. Carman, K. R. Barrie, G. Rebowski, R. Dominguez, Structures of the free and capped ends of the actin filament. *Science* **380**, 1287–1292 (2023).
21. R. Dominguez, K. C. Holmes, Actin structure and function. *Annu. Rev. Biophys.* **40**, 169–186 (2011).
22. R. Dominguez, Actin-binding proteins—A unifying hypothesis. *Trends Biochem. Sci.* **29**, 572–578 (2004).
23. M. H. Doran, M. J. Rynkiewicz, D. Rasicci, S. M. L. Bodt, M. E. Barry, E. Bullitt, C. M. Yengo, J. R. Moore, W. Lehman, Conformational changes linked to ADP release from human cardiac myosin bound to actin-tropomyosin. *J. Gen. Physiol.* **155**, e202213267 (2023).
24. R. P. Kapur, A. M. Goldstein, D. S. Loeff, C. T. Myers, C. R. Paschal, Intestinal pathology in patients with pathogenic ACTG2-variant visceral myopathy: 16 Patients from 12 families and review of the literature. *Pediatr. Dev. Pathol.* **25**, 581–597 (2022).
25. R. C. Robinson, M. Mejillano, V. P. Le, L. D. Burtnick, H. L. Yin, S. Choe, Domain movement in gelsolin: A calcium-activated switch. *Science* **286**, 1939–1942 (1999).
26. T. D. Pollard, Actin and actin-binding proteins. *Cold Spring Harb. Perspect. Biol.* **8**, a018226 (2016).
27. S. L. Brenner, E. D. Korn, The effects of cytochalasins on actin polymerization and actin ATPase provide insights into the mechanism of polymerization. *J. Biol. Chem.* **255**, 841–844 (1980).
28. D. Chereau, M. Boczkowska, A. Skwarek-Maruszewska, I. Fujiwara, D. B. Hayes, G. Rebowski, P. Lappalainen, T. D. Pollard, R. Dominguez, Leiomodin is an actin filament nucleator in muscle cells. *Science* **320**, 239–243 (2008).
29. V. M. Fowler, R. Dominguez, Tropomodulins and leiomodins: Actin pointed end caps and nucleators in muscles. *Biophys. J.* **112**, 1742–1760 (2017).
30. Y. Y. Toyoshima, S. J. Kron, E. M. McNally, K. R. Niebling, C. Toyoshima, J. A. Spudich, Myosin subfragment-1 is sufficient to move actin filaments in vitro. *Nature* **328**, 536–539 (1987).
31. P. W. Gunning, E. C. Hardeman, P. Lappalainen, D. P. Mulvihill, Tropomyosin—Master regulator of actin filament function in the cytoskeleton. *J. Cell Sci.* **128**, 2965–2974 (2015).
32. S. Pathan-Chhatbar, M. H. Taft, T. Reindl, N. Hundt, S. L. Latham, D. J. Manstein, Three mammalian tropomyosin isoforms have different regulatory effects on nonmuscle myosin-2B and filamentous β-actin in vitro. *J. Biol. Chem.* **293**, 863–875 (2018).
33. M. A. Geeves, S. E. Hitchcock-DeGregori, P. W. Gunning, A systematic nomenclature for mammalian tropomyosin isoforms. *J. Muscle Res. Cell Motil.* **36**, 147–153 (2015).
34. P. J. Carman, K. R. Barrie, R. Dominguez, Novel human cell expression method reveals the role and prevalence of posttranslational modification in nonmuscle tropomyosins. *J. Biol. Chem.* **297**, 101154 (2021).
35. S. Umemoto, J. R. Sellers, Characterization of in vitro motility assays using smooth muscle and cytoplasmic myosins. *J. Biol. Chem.* **265**, 14864–14869 (1990).
36. B. J. Perrin, J. M. Ervasti, The actin gene family: Function follows isoform. *Cytoskeleton* **67**, 630–634 (2010).
37. S. E. Bergeron, M. Zhu, S. M. Thiem, K. H. Friderici, P. A. Rubenstein, Ion-dependent polymerization differences between mammalian beta- and gamma-nonmuscle actin isoforms. *J. Biol. Chem.* **285**, 16087–16095 (2010).
38. M. Muller, R. P. Diensthuber, I. Chizhov, P. Claus, S. M. Heissler, M. Preller, M. H. Taft, D. J. Manstein, Distinct functional interactions between actin isoforms and nonsarcomeric myosins. *PLOS ONE* **8**, e70636 (2013).
39. H. Lu, P. M. Fagnant, E. B. Krementsova, K. M. Trybus, Severe molecular defects exhibited by the R179H mutation in human vascular smooth muscle α-actin. *J. Biol. Chem.* **291**, 21729–21739 (2016).
40. A. S. Kashina, Regulation of actin isoforms in cellular and developmental processes. *Semin. Cell Dev. Biol.* **102**, 113–121 (2020).
41. E. C. Hardeman, N. S. Bryce, P. W. Gunning, Impact of the actin cytoskeleton on cell development and function mediated via tropomyosin isoforms. *Semin. Cell Dev. Biol.* **102**, 122–131 (2020).
42. J. Chen, K. Kaw, H. Lu, P. M. Fagnant, A. Chattopadhyay, X. Y. Duan, Z. Zhou, S. Ma, Z. Liu, J. Huang, K. Kamm, J. T. Stull, C. S. Kwartler, K. M. Trybus, D. M. Milewicz, Resistance of $Acta2^{R149C/+}$ mice to aortic disease is associated with defective release of mutant smooth muscle alpha-actin from the chaperonin-containing TCP1 folding complex. *J. Biol. Chem.* **297**, 101228 (2021).
43. R. Dominguez, The WH2 domain and actin nucleation: Necessary but insufficient. *Trends Biochem. Sci.* **41**, 478–490 (2016).
44. H. J. Lehtonen, T. Sipponen, S. Tojkander, R. Karikoski, H. Jarvinen, N. G. Laing, P. Lappalainen, L. A. Aaltonen, S. Tuupanen, Segregation of a missense variant in enteric smooth muscle actin γ-2 with autosomal dominant familial visceral myopathy. *Gastroenterology* **143**, 1482–1491.e3 (2012).
45. D. Halim, R. M. Hofstra, L. Signorile, R. M. Verdijk, C. S. van der Werf, Y. Sribudiani, R. W. Brouwer, W. F. J. van IJcken, N. Dahl, J. B. Verheij, C. Baumann, J. Kerner, Y. van Bever, N. Galjart, R. M. Wijnen, D. Tibboel, A. J. Burns, F. Muller, A. S. Brooks, M. M. Alves, ACTG2 variants impair actin polymerization in sporadic megacystis microcolon intestinal hypoperistalsis syndrome. *Hum. Mol. Genet.* **25**, 571–583 (2016).
46. W. Thorson, O. Diaz-Horta, J. Foster II, M. Spiliopoulos, R. Quintero, A. Farooq, S. Blanton, M. Tekin, De novo ACTG2 mutations cause congenital distended bladder, microcolon, and intestinal hypoperistalsis. *Hum. Genet.* **133**, 737–742 (2014).
47. S. N. Chen, Y. Q. Wang, C. L. Hao, Y. H. Lu, W. J. Jiang, C. Y. Gao, M. Wu, Multisystem smooth muscle dysfunction syndrome in a Chinese girl: A case report and review of the literature. *World J. Clin. Cases* **7**, 4355–4365 (2019).
48. T. Oda, M. Iwasa, T. Aihara, Y. Maeda, A. Narita, The nature of the globular- to fibrous-actin transition. *Nature* **457**, 441–445 (2009).
49. B. Zhu, F. Daoud, S. Zeng, L. Matic, U. Hedin, B. Uvelius, C. Rippe, S. Albinsson, K. Sward, Antagonistic relationship between the unfolded protein response and myocardin-driven transcription in smooth muscle. *J. Cell. Physiol.* **235**, 7370–7382 (2020).
50. B. L. Eaton, Tropomyosin binding to F-actin induced by myosin heads. *Science* **192**, 1337–1339 (1976).
51. I. Ichetovkin, W. Grant, J. Condeelis, Cofilin produces newly polymerized actin filaments that are preferred for dendritic nucleation by the Arp2/3 complex. *Curr. Biol.* **12**, 79–84 (2002).
52. E. Andrianantoandro, T. D. Pollard, Mechanism of actin filament turnover by severing and nucleation at different concentrations of ADF/cofilin. *Mol. Cell* **24**, 13–23 (2006).
53. S. K. Hashmi, V. Barka, C. Yang, S. Schneider, T. M. Svitkina, R. O. Heuckeroth, Pseudo-obstruction-inducing ACTG2R257C alters actin organization and function. *JCI Insight* **5**, e140604 (2020).
54. H. Cai, Y. Xiao, S. Chen, Y. Lu, J. Du, Y. You, J. Zhu, J. Zhou, W. Cai, Y. Wang, Heterozygous $Actg2^{R257C}$ mice mimic the phenotype of megacystis microcolon intestinal hypoperistalsis syndrome. *Neurogastroenterol. Motil.* **35**, e14472 (2023).
55. H. Lu, P. M. Fagnant, C. S. Bookwalter, P. Joel, K. M. Trybus, Vascular disease-causing mutation R258C in ACTA2 disrupts actin dynamics and interaction with myosin. *Proc. Natl. Acad. Sci. U.S.A.* **112**, E4168–E4177 (2015).
56. J. D. Pardee, J. A. Spudich, Purification of muscle actin. *Methods Enzymol.* **85**, 164–181 (1982).
57. S. S. Rosenfeld, J. Xing, H. C. Cheung, F. Brown, S. Kar, H. L. Sweeney, Structural and kinetic studies of phosphorylation-dependent regulation in smooth muscle myosin. *J. Biol. Chem.* **273**, 28682–28690 (1998).

58. A. Drazic, H. Aksnes, M. Marie, M. Boczkowska, S. Varland, E. Timmerman, H. Foyn, N. Glomnes, G. Rebowski, F. Impens, K. Gevaert, R. Dominguez, T. Arnesen, NAA80 is actin's N-terminal acetyltransferase and regulates cytoskeleton assembly and cell motility. *Proc. Natl. Acad. Sci. U.S.A.* **115**, 4399–4404 (2018).
59. A. Punjani, H. Zhang, D. J. Fleet, Non-uniform refinement: Adaptive regularization improves single-particle cryo-EM reconstruction. *Nat. Methods* **17**, 1214–1221 (2020).
60. K. Naydenova, C. J. Russo, Measuring the effects of particle orientation to improve the efficiency of electron cryomicroscopy. *Nat. Commun.* **8**, 629 (2017).
61. Y. Z. Tan, P. R. Baldwin, J. H. Davis, J. R. Williamson, C. S. Potter, B. Carragher, D. Lyumkis, Addressing preferred specimen orientation in single-particle cryo-EM through tilting. *Nat. Methods* **14**, 793–796 (2017).
62. A. Casanal, B. Lohkamp, P. Emsley, Current developments in Coot for macromolecular model building of electron cryo-microscopy and crystallographic data. *Protein Sci.* **29**, 1069–1078 (2020).
63. G. C. P. van Zundert, N. W. Moriarty, O. V. Sobolev, P. D. Adams, K. W. Borrelli, Macromolecular refinement of X-ray and cryoelectron microscopy structures with Phenix/OPLS3e for improved structure and ligand quality. *Structure* **29**, 913–921.e4 (2021).
64. E. F. Pettersen, T. D. Goddard, C. C. Huang, E. C. Meng, G. S. Couch, T. I. Croll, J. H. Morris, T. E. Ferrin, UCSF ChimeraX: Structure visualization for researchers, educators, and developers. *Protein Sci.* **30**, 70–82 (2021).
65. I. Matera, M. Rusmini, Y. Guo, M. Lerone, J. Li, J. Zhang, M. Di Duca, P. Nozza, M. Mosconi, A. Pini Prato, G. Martucciello, A. Barabino, F. Morandi, R. De Giorgio, V. Stanghellini, R. Ravazzolo, M. Devoto, H. Hakonarson, I. Ceccherini, Variants of the ACTG2 gene correlate with degree of severity and presence of megacystis in chronic intestinal pseudo-obstruction. *Eur. J. Hum. Genet.* **24**, 1211–1215 (2016).
66. H. Lee, S. Park, J. T. Oh, H. M. Kim, S. Kim, J. S. Lee, Oral pyridostigmine-responsive visceral myopathy with ACTG2 mutations: A case series. *J. Pediatr. Gastroenterol. Nutr.* **68**, e16–e17 (2019).
67. G. Ravenscroft, S. Pannell, G. O'Grady, R. Ong, H. C. Ee, F. Faiz, L. Marns, H. Goel, P. Kumarasinghe, E. Sollis, P. Sivadorai, M. Wilson, A. Magoffin, S. Nightingale, M. L. Freckmann, E. P. Kirk, R. Sachdev, D. A. Lemberg, M. B. Delatycki, M. A. Kamm, C. Basnayake, P. J. Lamont, D. J. Amor, K. Jones, J. Schilperoort, M. R. Davis, N. G. Laing, Variants in ACTG2 underlie a substantial number of Australasian patients with primary chronic intestinal pseudo-obstruction. *Neurogastroenterol. Motil.* **30**, e13371 (2018).
68. B. K. Brar, K. Blakemore, C. Hertenstein, J. L. Miller, K. A. Miller, H. Shamseldin, S. Maddirevula, T. Hays, B. Lianoglou, S. Dukhovny, L. A. Baker, T. N. Sparks, R. Wapner, F. S. Alkuraya, M. E. Norton, A. C. Jelin; Fetal Sequencing Consortium, The utility of gene sequencing in identifying an underlying genetic disorder in prenatally suspected lower urinary tract obstruction. *Prenat. Diagn.* **44**, 196–204 (2024).
69. A. Milunsky, C. Baldwin, X. Zhang, D. Primack, A. Curnow, J. Milunsky, Diagnosis of chronic intestinal pseudo-obstruction and megacystis by sequencing the ACTG2 gene. *J. Pediatr. Gastroenterol. Nutr.* **65**, 384–387 (2017).
70. R. Krabek, V. M. Smed, E. Oestergaard, K. Sundberg, Variant in ACTG2 causing megacystis microcolon hypoperistalsis syndrome and severe familial postpartum bleeding. *Fetal Diagn. Ther.* **49**, 491–495 (2023).
71. A. Milunsky, J. Lazier, C. Baldwin, C. Young, D. Primack, J. M. Milunsky, Prenatal diagnosis of chronic intestinal pseudo-obstruction and paternal somatic mosaicism for the ACTG2 pathogenic variant. *Prenat. Diagn.* **37**, 1254–1256 (2017).
72. K. Ignasiak-Budzynska, M. Danko, J. Ksiazyk, Megacystis-microcolon-intestinal hypoperistalsis syndrome (MMIHS): Series of 4 cases caused by mutation of ACTG2 (actin gamma 2, smooth muscle) gene. *Case Rep. Gastrointest. Med.* **2021**, 6612983 (2021).
73. J. W. Hahn, S. Y. Moon, M. S. Kim, M. H. Woo, M. J. Sohn, H. Y. Kim, M. W. Seong, S. S. Park, S. H. Park, J. S. Moon, J. S. Ko, ACTG2 variants in pediatric chronic intestinal pseudo-obstruction with megacystis. *J. Neurogastroenterol. Motil.* **28**, 104–110 (2022).
74. W. Dong, C. Baldwin, J. Choi, J. M. Milunsky, J. Zhang, K. Bilguvar, R. P. Lifton, A. Milunsky, Identification of a dominant MYH11 causal variant in chronic intestinal pseudo-obstruction: Results of whole-exome sequencing. *Clin. Genet.* **96**, 473–477 (2019).
75. Z. Wei, L. Lu, Y. Zheng, W. Yan, Y. Tao, Y. Xiao, W. Cai, Y. Wang, Variants in the enteric smooth muscle actin γ-2 cause pediatric intestinal pseudo-obstruction in Chinese patients. *J. Pediatr. Gastroenterol. Nutr.* **72**, 36–42 (2021).
76. R. R. J. Collins, B. Barth, S. Megison, C. M. Pfeifer, L. M. Rice, S. Harris, C. F. Timmons, D. Rakheja, ACTG2-associated visceral myopathy with chronic intestinal pseudoobstruction, intestinal malrotation, hypertrophic pyloric stenosis, choledochal cyst, and a novel missense mutation. *Int. J. Surg. Pathol.* **27**, 77–83 (2019).
77. O. L. Holla, G. Bock, O. L. Busk, B. L. Isfoss, Familial visceral myopathy diagnosed by exome sequencing of a patient with chronic intestinal pseudo-obstruction. *Endoscopy* **46**, 533–537 (2014).
78. C. A. Moreno, K. Metze, E. A. Lomazi, D. R. Bertola, R. H. Barbosa, V. Cosentino, N. Sobreira, D. P. Cavalcanti, Visceral myopathy: Clinical and molecular survey of a cohort of seven new patients and state of the art of overlapping phenotypes. *Am. J. Med. Genet. A* **170**, 2965–2974 (2016).
79. C. Billon, A. Molin, C. Poirsier, A. Clemenson, C. Dauge, M. Grelet, S. Sigaudy, S. Patrier, A. Goldenberg, V. Layet, J. Tantau, C. Fleury, A. Liard, A. Diguet, R. Fritih, E. Verspyck, J. Rendu, L. Boutaud, A. Tessier, S. Thomas, F. Razavi, A. Achaiaa, N. Elkhartoufi, L. Hakkakian, E. Magnin, C. Bole-Feysot, C. Masson, Y. Ville, P. Roth, F. Prieur, B. Bessieres, M. Bonniere, T. Attie-Bitach, Fetal megacystis-microcolon: Genetic mutational spectrum and identification of PDCL3 as a novel candidate gene. *Clin. Genet.* **98**, 261–273 (2020).
80. N. S. Sandy, K. Huysentruyt, D. J. Mulder, N. Warner, K. Chong, C. Morel, S. AlQahtani, P. W. Wales, M. G. Martin, A. M. Muise, Y. Avitzur, The diverse phenotype of intestinal dysmotility secondary to ACTG2-related disorders. *J. Pediatr. Gastroenterol. Nutr.* **74**, 575–581 (2022).
81. L. Tuzovic, S. Tang, R. S. Miller, L. Rohena, L. Shahmirzadi, K. Gonzalez, X. Li, C. A. LeDuc, J. Guo, A. Wilson, A. Mills, K. Glassberg, H. Rotterdam, A. R. Sepulveda, W. Zeng, W. K. Chung, K. Anyane-Yeboa, New insights into the genetics of fetal megacystis: ACTG2 mutations, encoding γ-2 smooth muscle actin in megacystis microcolon intestinal hypoperistalsis syndrome (Berdon syndrome). *Fetal Diagn. Ther.* **38**, 296–306 (2015).
82. E. U. Korgali, A. Yavuz, C. E. C. Simsek, C. Guney, H. K. Kurtulgan, B. Baser, M. H. Atalar, H. Ozer, H. R. Egilmez, Megacystis microcolon intestinal hypoperistalsis syndrome in which a different de novo Actg2 gene mutation was detected: A case report. *Fetal Pediatr. Pathol.* **37**, 109–116 (2018).
83. X. Xiong, J. Li, C. Liu, F. Xu, Visceral myopathy diagnosed by a de novo ACTG2 mutation in a patient with chronic intestinal pseudo-obstruction-a case report. *Transl. Pediatr.* **10**, 679–685 (2021).
84. Z. Stark, T. Y. Tan, B. Chong, G. R. Brett, P. Yap, M. Walsh, A. Yeung, H. Peters, D. Mordaunt, S. Cowie, D. J. Amor, R. Savarirayan, G. McGillivray, L. Downie, P. G. Ekert, C. Theda, P. A. James, J. Yaplito-Lee, M. M. Ryan, R. J. Leventer, E. Creed, I. Macciocca, K. M. Bell, A. Oshlack, S. Sadedin, P. Georgeson, C. Anderson, N. Thorne; Melbourne Genomics Health Alliance, C. Gaff, S. M. White, A prospective evaluation of whole-exome sequencing as a first-tier molecular test in infants with suspected monogenic disorders. *Genet. Med.* **18**, 1090–1096 (2016).
85. J. R. Whittington, A. T. Poole, E. H. Dutta, M. B. Munn, A novel mutation in ACTG2 gene in mother with chronic intestinal pseudoobstruction and fetus with megacystis microcolon intestinal hypoperistalsis syndrome. *Case Rep. Genet.* **2017**, 9146507 (2017).
86. W. Lu, Y. Xiao, J. Huang, Y. Tao, W. Yan, L. Lu, Y. Cao, W. Cai, Mutation in actin γ-2 responsible for megacystis microcolon intestinal hypoperistalsis syndrome in 4 Chinese patients. *J. Pediatr. Gastroenterol. Nutr.* **63**, 624–626 (2016).
87. M. X. Shen, C. Zhao, Y. J. Wang, X. W. Xin, Y. Yin, Y. P. Jin, ACTG2 associated visceral myopathy with intestinal pseudoobstruction. *Zhonghua Er Ke Za Zhi* **59**, 331–333 (2021).
88. M. Topa, L. Porcaro, G. Basilisco, A young woman with chronic intestinal pseudo-obstruction since birth. *Gastroenterology* **165**, 1338–1341 (2023).
89. J. Klar, D. Raykova, E. Gustafson, I. Tothova, A. Ameur, A. Wanders, N. Dahl, Phenotypic expansion of visceral myopathy associated with ACTG2 tandem base substitution. *Eur. J. Hum. Genet.* **23**, 1679–1683 (2015).

Acknowledgments: We thank D. Safer and R. Wike for the expression and purification of SMM-S1 and C. Pai for help with the statistical analysis of the data. **Funding:** This work was supported by the National Institutes of Health [grants R01 GM073791 (R.D.), R37 GM057247 (E.M.O.), R01 DK128282 (R.O.H.), F31 DK127610 (R.H.C.), and T32 AR053461 (N.J.P.)]. **Author contributions:** Writing—original draft: R.H.C., E.M.O., and R.D. Conceptualization: R.H.C., P.J.C., R.O.H., E.M.O., and R.D. Investigation: R.H.C., F.A.B.-C., N.J.P., P.J.C., and R.D. Writing—review and editing: R.H.C., P.J.C., R.O.H., E.M.O., and R.D. Methodology: F.A.B.-C., P.J.C., M.B., R.O.H., E.M.O., and R.D. Resources: F.A.B.-C., P.J.C., and R.O.H. Funding acquisition: R.H.C., R.O.H., E.M.O., and R.D. Validation: R.H.C., F.A.B.-C., P.J.C., M.B., R.O.H., E.M.O., and R.D. Supervision: R.O.H., E.M.O., and R.D. Formal analysis: R.H.C., F.A.B.-C., P.J.C., M.B., and E.M.O. Project administration: R.O.H., E.M.O., and R.D. Visualization: R.H.C., F.A.B.-C., N.J.P., P.J.C., E.M.O., and R.D. **Competing interests:** The authors declare that they have no competing interests. **Data and materials availability:** All the data needed to evaluate the conclusions in the paper are present in the paper and/or the Supplementary Materials. Cryo-EM maps of filaments of ACTG2 WT, R40C, and R257C have been deposited in the Electron Microscopy Data Bank with accession codes EMD-42918, EMD-42939, and EMD-42938, respectively, and atomic models have been deposited in the PDB with accession codes 8V2O, 8V30, and 8V27.

Submitted 20 December 2023
Accepted 29 April 2024
Published 31 May 2024
10.1126/sciadv.adn6615